Authors' Accepted Manuscript of paper accepted for publication by Tribology International,
DOI: https://doi.org/10.1016/j.triboint.2025.111327

Methods for determining contact stiffness and damping characteristics of individual railway ballast grains

Tianqi Zhang[a,b,c,d], David Thompson[b], William Powrie[c], Louis Le Pen[c], Madhu Murthy[c], Jacapo Piazza[c], Yanyun Luo[d]

a. *State Key Laboratory of Mechanical System and Vibration, School of Mechanical Engineering, Shanghai Jiao Tong University, Shanghai 200240, China*
b. *Institute of Sound and Vibration Research, University of Southampton, Southampton SO17 1BJ, UK*
c. *School of Engineering, University of Southampton, Southampton SO17 1BJ, UK*
d. *College of Transportation, Tongji University, Shanghai 201804, China*

Abstract

The macroscopic dynamic behaviour of granular systems composed of ballast particles is closely related to their mesoscopic contact characteristics, such as contact stiffness and damping between individual pairs of ballast particles. Existing studies primarily conduct macroscopic-level comparisons between simulations and experiments to calibrate the parameters of ballast groups or layers. In this work, mesoscopic contact tests were conducted to investigate the contact behaviour of individual ballast grains with different particle size and service condition. Analysis methods are proposed to extract the nonlinear stiffness behaviour from the hysteresis curves as well as the corresponding damping ratios. These methods are verified using simple theoretical modelling of Hertzian nonlinear behaviour with damping. A correction method is proposed to account for plastic deformation.

Key words

Ballast grains; Uniaxial compression; Hertzian contact; Damping ratio

1 Introduction

Although ballastless railway track has increased in popularity in recent years, ballasted track is still a very common form [1-3]. The ballasted track is mainly composed of the sleepers and the crushed stone ballast bed, which transfers load to the subgrade [4-5]. Compared with the ballastless track, energy dissipation through interactions between the ballast grains is a significant advantage of the ballasted track

[6-8]. Under long-term loading, the ballast grains experience abrasion, crushing, and pulverization, affecting the mechanical properties, including contact stiffness, damping ratio, friction [9], surface degradation [10], shape [11], time-dependent plasticity [12], rotational resistance [13] and others, thereby resulting in the degradation of the mechanical performance of the ballasted track [10-16]. Evaluating the mechanical properties of fresh and used ballast particles offers essential insights for enhancing maintenance strategies, ensuring track stability, and sustainable management of railway infrastructure [17-18].

The macroscopic dynamic characteristics of ballasted track are determined by the mesoscopic ballast particles and the interactions between them, thus the discrete element method (DEM) is suitable for mechanical analysis of railway ballast [19-24]. However, definition of the grain-scale input parameters requires care, particularly the contact stiffness and damping, which have a major influence on the overall constitutive behaviour of the ballast. In general, it is necessary to define the contact behaviour between grains, including the normal and shear contact stiffnesses, friction coefficient and contact damping, and the properties of the grains themselves, such as density, size and shape. The grain scale parameters required for DEM are mostly obtained indirectly by calibration; that is, comparing the macroscopic behaviour of a DEM model to that obtained in experiments on assemblies of grains with similar boundary conditions, and adjusting the grain scale parameters until similar results are achieved [25-30]. However, this is prone to error. Direct experiments at the grain scale would be preferable, but need to be specific to the type of crushed rock and are not always possible [9, 31]. There may also be an inherent variability in contact characteristics that is difficult to capture in a universal model.

The normal and tangential contact stiffness behaviour between individual grains is important for the dynamic interaction between particles. Table A1 in the Appendix A summarises the contact models, parameters and corresponding model calibration tests reported in the literature for modelling ballast using DEM. In DEM simulations of railway ballast, a linear contact model is most commonly used for both normal and tangential stiffness [32-41], although the nonlinear Hertzian contact model is also adopted by some authors [25, 42-45]. The conical damage model (CDM) [46-48] and the rolling resistance linear model (RRLM) [38, 49, 50] are also used in some cases. Sliding of one grain relative to another is governed by a friction coefficient. The normal or tangential contact stiffnesses and the friction coefficient are usually calibrated with reference to macroscopic experiments including shear tests [32, 33], box tests [19, 34-36, 42] and uniaxial or triaxial compression tests [37, 51, 52].

The contact stiffness value is also commonly calibrated by comparison with dynamic experiments of ballast particle groups or ballast layers. The stiffness values used vary over a large range, from 0.6 to 2000 MN/m for the linear contact model, as shown in Table A1. These large differences may be related to the test boundary conditions and the rock type. The ratio of tangential to normal stiffness is usually chosen to be close to 1.0. The stiffness parameters used in the Hertzian contact model [53] also vary over a wide range [25, 42-45, 55].

In the research summarised above, the required mesoscopic contact properties of individual grains are derived indirectly from the macro-level dynamic behaviour of ballast grain groups. There is a lack of direct investigations of the contact behaviour between the grains and the corresponding stiffness values.

Additionally, the damping properties also play a key role in ballast track dynamic characteristics, especially energy dissipation [56]. The energy dissipation in DEM modelling of ballast grains is specified as local damping and viscous damping [40, 56]. Local damping acts as a particle attribute, not a contact model parameter, applying a damping force to each particle proportional to the unbalanced force, and is controlled by the damping constant. Values of local damping, used in DEM to suppress oscillations, vary from 0.7 [42] to 0.2 [40] and 0.05 [25]. In contrast, viscous damping is applied at each contact by incorporating a dashpot parallel to the contact model, defined by the contact damping ratio.

The current primary methodologies for determining the contact damping ratio can be categorized into four distinct approaches: (i) derivation from the phase angle of the dynamic stiffness through laboratory-based measurement of the dynamic stiffness of ballast layers [57]; (ii) fitting of the time history curves of the free vibration response [58, 59] through experimental analysis involving impact hammer tests and loading tests on single ballast particles and in ballasted track; (iii) calibration by comparing the translational acceleration of the ballast particle of a DEM simulation model with a full-scale laboratory test of ballasted track [40]; (iv) calculation as the ratio of dissipated energy to stored energy during each loading-unloading cycle based on a cyclic loading box test [60]. The experimental investigations on ballast damping ratio yield a wide range of values across different studies, from 0.01 to 0.8 [34, 40, 56-63]. In summary, the existing methods of obtaining contact damping ratio are mostly based on the comparison of simulation and experiment at the macro level. individual ballast grains. There are few studies on the meso-contact damping characteristics between individual ballast particles.

The aim of the current work is to investigate and develop methods for determining the nonlinear stiffness and equivalent damping characteristics of the contact between individual ballast grains at a meso-level from measurements of their normal load-deflection behaviour. While previous studies have investigated the contact stiffness and damping ratio of ballast [43, 64-66], this work further examines them for point-to-point contact of ballast with different grain sizes. The nonlinear contact stiffness is derived from stabilized cyclic loading data to minimize plastic deformation effects. Furthermore, a new damping ratio estimation method is proposed that incorporates the nonlinear stiffness characteristics of ballast contact and a correction is introduced to allow for plastic deformation, thereby providing a more accurate characterization of ballast contact behavior. It should be noted that this study focuses exclusively on the normal contact stiffness and damping among the many key characteristics of the complex contact system of ballast particles, providing a tractable and quantifiable starting point for particle-scale parameter identification. Nevertheless, as noted above, ballast particles exhibit highly nonlinear behavior, and their contacts are governed by more complex mechanisms, including friction, surface degradation, time-dependent plasticity, rotational resistance and other mechanisms. Further research is needed to capture these effects and establish a comprehensive framework for describing ballast contact behavior.

Based on this, uniaxial compression tests are conducted on eight examples of pairs of ballast grains with different particle sizes and different service life. Analysis methods are developed to extract the mesoscopic nonlinear contact stiffness behaviour from the load-displacement curves. Damping characteristics are quantified in terms of an equivalent contact damping ratio. The method for determining this is adapted to take account of the nonlinear stiffness behaviour and the effect of non-closure of the hysteresis loops. As the overall mechanical behaviour of ballasted track in numerical simulations is predominantly determined by the contacts between individual ballast particles, the contact behaviour and properties obtained from the uniaxial compression test of individual railway ballast grains are helpful for a deeper understanding of the mechanics and energy dissipation characteristics of ballasted track.

2 Uniaxial compression tests of ballast grains

To study the contact stiffness and damping characteristics of individual pairs of ballast grains, uniaxial compression tests are conducted on eight example pairs of fresh and used granite ballast particles with different particle sizes under cyclic loading and unloading conditions. During the test, the magnitude of the load applied by the apparatus and the vertical relative displacement of the ballast are recorded over 10 cycles of loading and unloading. Based on the recorded data, the load-displacement curve results of all ballast pairs are obtained and used to analyse their contact characteristics. Considering the high heterogeneity of ballast particles, repeated tests were conducted on these eight pairs of particles, and the load-displacement results under different particle orientations (a total of 21 sets of tests) were also analysed to study a wider range of interactions.

2.1 Test specimens and procedure

To investigate the contact characteristics of ballast grains, pairs of ballast grains of similar sizes were selected [67]. Four pairs were of fresh, crushed granite, obtained from Cliffe Hill quarry (Leicestershire, UK), the mineralogical composition of which is described by Abadi et al. [3]. The other four pairs were of used granite ballast grains that had been recovered from a track bed during renewal works. It is thought to have been in the track bed for up to 30 years, during which time it was subjected to many millions of cycles of train axle loading and more than 15 tamping maintenance cycles.

In [68], Gupta et al. compared the particle characteristics of fresh and used ballast through the Micro - Deval apparatus and the Los Angeles abrasion test. With trafficking and/or tamping, the individual grains tend to wear, and the used ballast was found to be less angular than fresh ballast. Tutumluer et al. [69] conducted comprehensive tests on fresh and used ballast, including morphological characterization, mechanical breakdown, and degradation performance. They found that used ballast exhibits more wear on the surface and less angularity. Based on this, although this study did not directly measure changes to the stiffness characteristics under long-term loading conditions, the influence of cumulative effects such as wear and fatigue on the stiffness was indirectly considered by comparing the behaviour of fresh and used ballast. Comparing fresh and used ballast grains is considered as a practical approach to study the possible evolution of stiffness over time without the need to apply very large numbers of loading cycles.

The samples were selected to cover the range of sizes typically found in the gradation of ballast used by the railways, defined by different sieve sizes. For ease of presentation later, the fresh ballast grains of different sizes are identified as letters A-D and the used ballast as letters G-K. In addition, considering the high non-uniformity and roughness of the ballast surface, the orientation of ballast grains also affects the contact area, slippage and other characteristics of the ballast. Therefore, on the basis of repeated tests, the load-displacement characteristics under different contact directions were also tested. For the convenience of distinction, the test code is named *TiOj (where * (= A, B, C, D, G, H, I, K) represents fresh and used ballast particles of different particle sizes, Ti (i = 1, 2) represents the number of the tests, and Oj (j = 1, 2) represents the ballast grain orientations. The particle sizes and test codes of the tested ballast grains are listed in Table 1. It should be noted that the tests labelled BT1O2, CT1O2, and DT1O2 yielded unreliable results due to unstable contact and excessive shear and are not considered. Thus, a total of 21 tests were conducted, including repeat measurements of all eight particle pairs and five tests performed by re-orienting the original eight particle pairs. Although these combinations are not fully independent, the number of effectively independent contact conditions is 13, which is consistent with previous studies [31, 65]. Together with careful particle selection, relatively uniform material properties, moderate cyclic loads (5-200 N) unlikely to induce significant internal damage, and a focus on converged responses over later cycles, this helps to ensure that the results are reliable and representative of the behavior of typical ballast particles.

Table 1. Size and test code summaries of fresh and used ballast grains

Sieve size (mm)	Fresh ballast	Used ballast
50.0	AT1O1; AT2O1; AT1O2	GT1O1; GT2O1; GT1O2
40.0	BT1O1; BT2O1	HT1O1; HT2O1; HT1O2
31.5	CT1O1; CT2O1	IT1O1; IT2O1; IT1O2
22.4	DT1O1; DT2O1	KT1O1; KT2O1; KT1O2

The test method [67] is adapted from the approach of Cole & Peters [71], who performed normal contact experiments on pairs of small unbonded grains of gneiss, Ottawa sand, and lunar simulants [72]. It is focused on the examination of the load-deflection behaviour in the direction normal to the contact. To prevent the grains from rotating during testing, they were fixed into a holder using resin, as shown in Fig. 1. The load was applied to the ballast grains using an Instron 5569 electromechanical uniaxial test machine and measured using a vertical force sensor with a range of 500 N. The relative displacement of the grains in the axial direction was measured using two high resolution cameras placed at a 90-degree angle to the contact interface. The upper ballast stone was brought into contact with the lower one, and a small (< 0.5 N) bedding load was applied. The load was increased at a rate of 1 N/s to 5 N, where it was held constant for 30 s to ensure stable contact. The load was then cycled between 5 N and 200 N at a rate of 4 N/s for 10 cycles, pausing at the end of each loading or unloading stage for 97.5 s. The entire loading / unloading sequence was filmed at 30 frames per second (fps) using the high-resolution cameras. The images of each frame were analysed using a digital image correlation algorithm (DIC) [67, 73, 74] to determine the relative movement of the grains. Further details of the test equipment, procedures, and methodology can be found in the previous publication [67]. To first verify the reliability of the experimental setup and underlying theory, tests were conducted on spherical steel grains. The results confirmed both the accuracy of the spatial measurement resolution and the validity of Hertzian contact theory in predicting deflections under known forces [67]. Once the test concept was validated, experiments were then performed on real ballast grains.

Fig. 1 Uniaxial compression test of railway ballast grains. Ballast samples A are shown mounted in resin and brought into contact.

2.2 Test results of load-displacement curves

Fig. 2 shows the load-displacement curves for the eight pairs of fresh and used ballast grains in the initial orientation during loading and unloading over 10 loading cycles. The displacement here refers to the relative displacement between the ballast pairs. Fig. 2(a) shows the load-displacement curves for the 50 mm fresh ballast pair labelled A as an example, in which each load cycle is highlighted in a different colour. In each cycle, the unloading curve lies below the preceding loading curve, forming a hysteresis loop indicating energy loss. Moreover, the hysteresis loop is usually not closed, with the degree of non-closure reflecting the magnitude of the residual plastic strain occurring over the load cycle. The test results for the other ballast pairs B-K in the initial orientation, shown in Fig. 2(b)-(h), have similar behaviour. In addition, the force-displacement results of uniaxial compression tests in other particle orientation show similar characteristics.

To quantify the residual plastic strain characteristics of fresh and used ballast pairs with different particle sizes during cyclic loading and unloading, the residual plastic strain values after each cycle are extracted from the load-displacement curves of the 21 tests, as shown in Fig. 3. Except for the second cycle of ballast A and K, the residual plastic deformation within each cycle decreases with increasing number of cycles, as the contacts gradually stabilize. In particular, by the end of most tests, for example, in the case of ballast pairs A, the particle surfaces exhibited a thin coating of fine powder, indicating that microscale asperity damage had taken place. A more rigorous characterization of this phenomenon could be achieved through microscopic observations in the future, enabling quantitative evaluation of surface roughness alterations during the loading process.

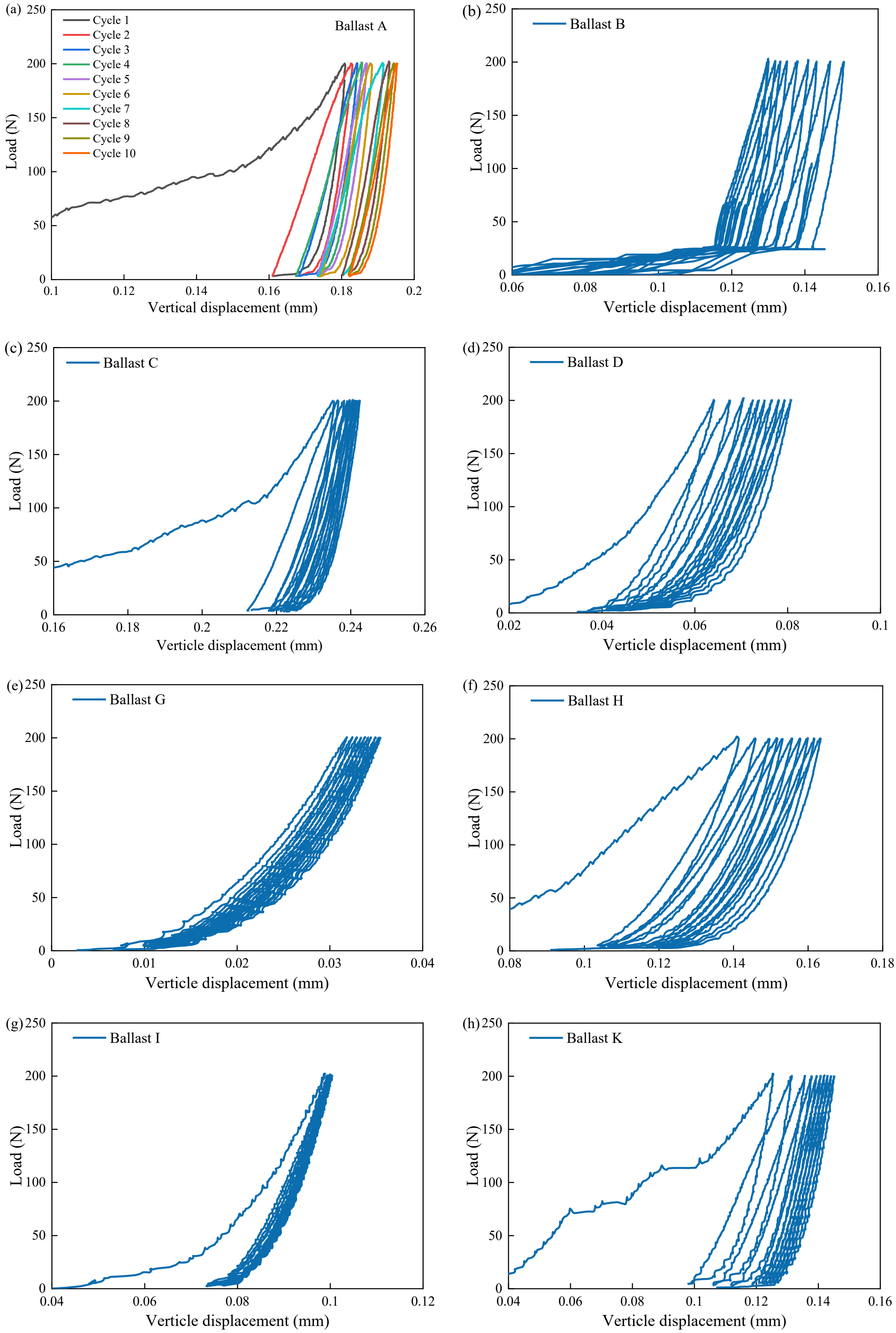

Fig. 2 Load-displacement curves of ballast samples. (a) Ballast pair A, (b) ballast pair B, (c) ballast pair

C, (d) ballast pair D, (e) ballast pair G, (f) ballast pair H, (g) ballast pair I, (h) ballast pair K.

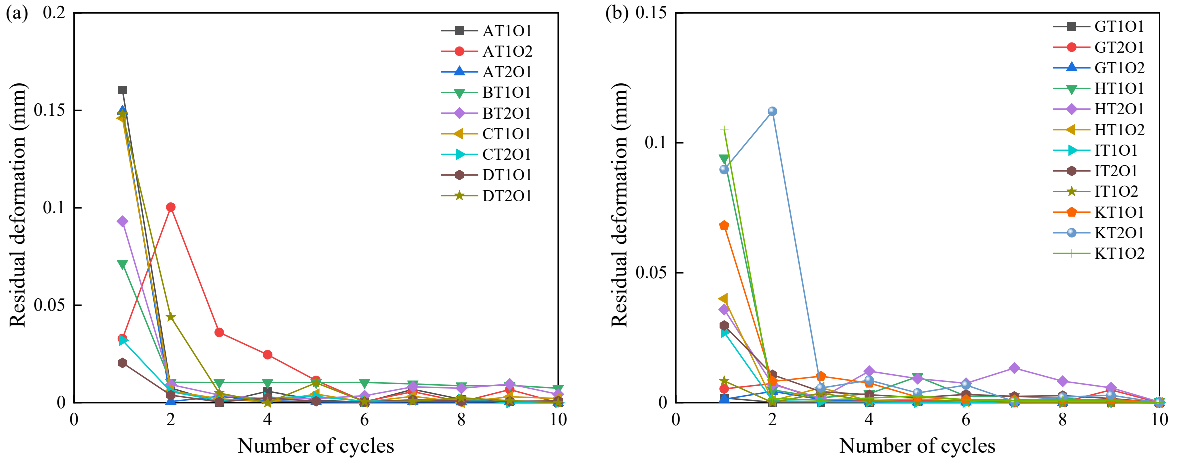

Fig. 3 Residual plastic strain values after each cycle. (a) Fresh ballast pairs A-D; (b) Used ballast pairs G-K.

3 Contact stiffness characteristics and parameters

Based on the measured load - displacement curves of ballast grains obtained in the uniaxial compression tests in Section 2, a procedure is developed to extract the nonlinear contact stiffness characteristics. These mesoscopic contact behaviour and parameters can be used as a reference for the micromechanical characteristics and the input parameters of the numerical simulation.

3.1 Nonlinear contact stiffness characteristics

In a previous paper [67], it was shown that Hertzian nonlinear contact [53, 54] could be used to represent the global contact behaviour between ballast grains, but the contact radii required were found to change with different load steps. Here, a new method is used to investigate the contact characteristics by first removing the hysteretic effect, and simplified contact parameters are obtained which can also be used as a reference for the input parameters of DEM simulations. The focus is on the global stiffness behaviour of the two ballast grains in contact, not on the local behaviour at the contact interface.

The average curve between the loading and unloading curves is used to exclude the hysteresis effect and to represent the underlying elastic characteristics of the system. These curves are then fitted with a suitable power law function to obtain the contact behaviour and associated parameters. The ninth cycle is used as it can be seen from Fig. 2 that there is minimal residual strain by the time this cycle is reached. The starting point of each loop is normalised to correspond to a deflection of 0.

Taking pairing A as an example, a power law function of the form

$$F = G_0^* x^n \tag{1}$$

is sought, where F is the load, x is the deflection, n is an exponent and G_0^* is a nonlinear stiffness coefficient. This function is used to fit the average curve, as shown in Fig. 4(a). R^2 is the regression coefficient, which refers to the degree of fit of the regression line to the observed values; the closer the value of R^2 is to 1, the better the fit of the regression curve. The value of R^2 of the fitted curve for ballast A is 0.9982, which is very close to 1; the fitted function is $y=2.424\times10^5\times x^{1.617}$. Applying the same procedure to the other ballast pairs and repeated tests (not shown, a total of 21 tests) gave results for the exponent n that are between 1.31 and 1.70. These exponents are all close to 1.5, which corresponds to Hertzian contact, and despite minor variations, the regression coefficients for the set of tests were above 0.96.

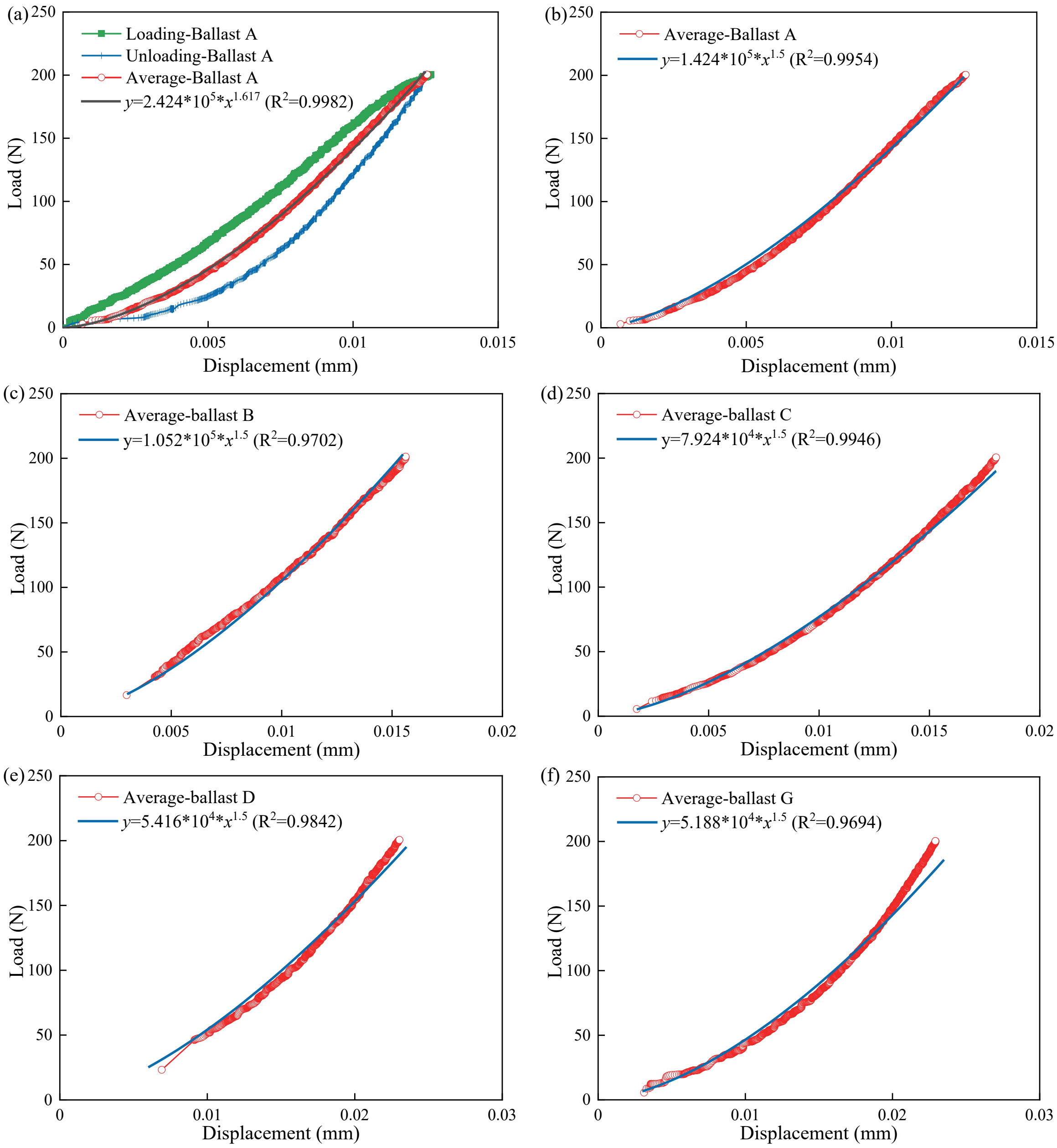

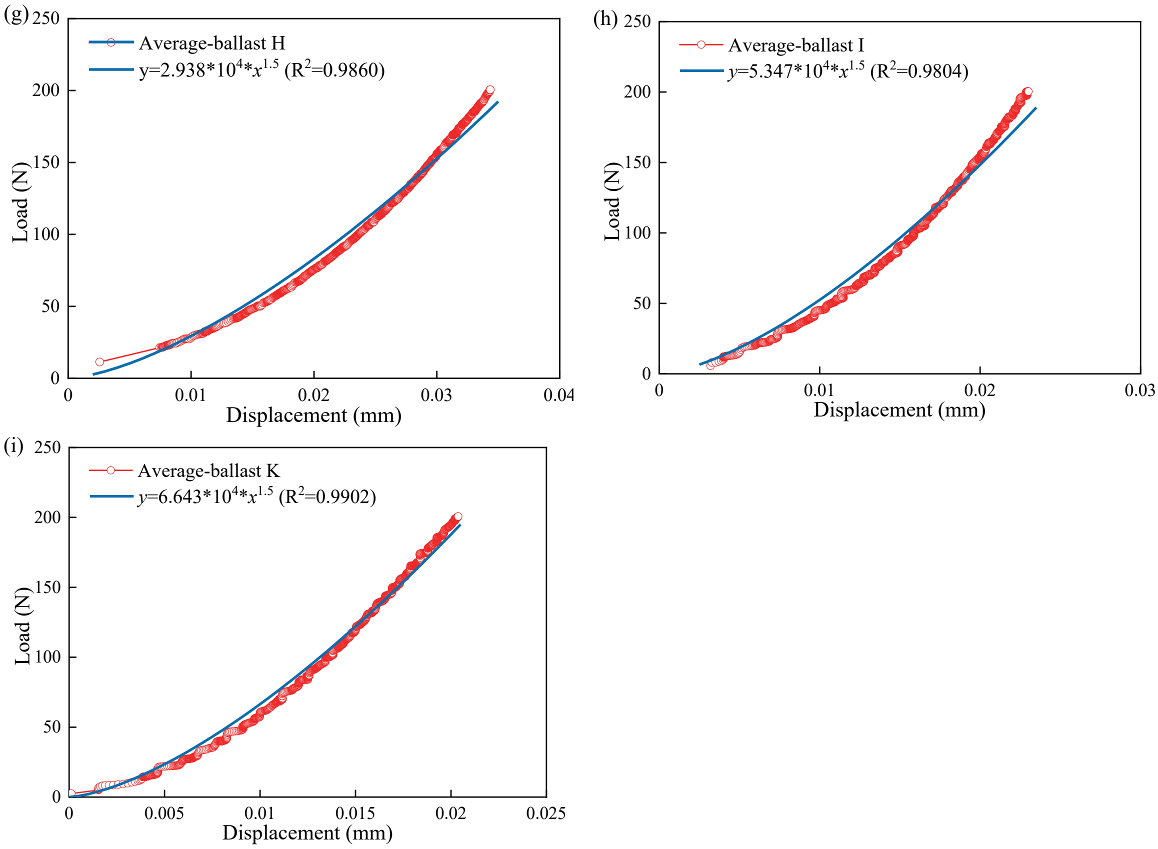

Fig. 4 The load-displacement curve and fitted function of ballast samples A-K in their 9th cycle. (a) The loading, unloading and average load-displacement curves of ballast sample A, with fitted curve for arbitrary value of exponent n. (b) The fitted power law function of the average load-displacement curve of ballast sample A for n=1.5. (c)-(i) The fitted power law functions of the average load-displacement curves of ballast samples B-K for n=1.5.

3.2 Hertzian contact stiffness parameters

According to Hertzian theory [53, 54, 67], for two spheres in contact, the normal force F required to produce a displacement x is given by:

$$F = \frac{4}{3}\sqrt{r}E^{*}x^{\frac{3}{2}}, \tag{2}$$

$$E^{*} = \left(\frac{1-v_1^2}{E_1} + \frac{1-v_2^2}{E_2}\right)^{-1}, \tag{3}$$

$$r = \left(\frac{1}{r_1} + \frac{1}{r_2}\right)^{-1}, \tag{4}$$

where E^* is an equivalent elastic modulus. E_1 and E_2 are the Young's moduli, and v_1 and v_2 the Poisson's ratios of the two spheres. r is the effective radius of the contacting surfaces, while r_1 and r_2 are the radii of the two spheres.

In this paper, the ballast grains tested are assumed to have the same Young's modulus and Poisson's ratio. Static properties for granite are given in Ref. [75]. These can vary between samples of apparently similar rock, even from the same quarry, but the literature suggests a typical Young's modulus E of 64 GPa and Poisson's ratio v of 0.176 [67]. From Eq. (3) this gives an equivalent elastic modulus E* of 33.0 GPa. Compared with existing studies (see Table A1), the shear modulus and Poisson's ratio of ballast fall within a reasonable range. To obtain the correct contact parameter G^* for use in a Hertzian model, n in Eq. (1) is next constrained to be equal to 1.5 and then the average load-displacement curve is fitted with the power law function, which gives the results shown in Table 2. The fitted curves are shown in Fig. 4(b)-(i) for the eight ballast pairs in the initial orientation. The regression coefficients R^2 are all greater than 96%, which means that the fitted function is credible. The values of G^* with n = 1.5 should be equal to $4/3\sqrt{r}E^*$ (see Eq. (2)). Using the value for E^*, the effective radius r of all the tested ballast particles can be estimated, as listed in Table 2. It can be seen that the effective contact radii of the fresh ballast grains range from 1.313 mm to 11.41 mm with different particle size, while those for used ballast grains vary from 0.446 mm to 2.704 mm. The same pair of ballast grains showed a generally consistent response across different test groups, with the discrepancies caused by the nonlinear contact behavior remaining within an acceptable range.

It should be emphasized that the results presented in this section demonstrate that the contact behavior between ballast particles conforms to the nonlinear Hertzian contact. In DEM simulations, various contact models are typically employed, including linear, Hertzian nonlinear, linear bond, and hysteretic models. The conclusion obtained here can thus be directly used as an input for contact model in DEM analyses of ballast mechanical behavior. Moreover, the nonlinear Hertzian contact model in DEM generally requires parameters such as Young's modulus, Poisson's ratio, and the power-law exponent, and the corresponding values identified in this section (64 GPa, 0.176 and 1.5) can be adopted as model inputs.

Table 2. Nonlinear stiffness coefficient and corresponding effective radii in Hertzian contact obtained from fitting average load-displacement curves (cycle 9, n set as 1.5)

Sieve size (mm)	Fresh ballast	G^* (N/mm$^{1.5}$)	R^2	r (mm)	Used ballast	G^* (N/mm$^{1.5}$)	R^2	r (mm)
50.0	AT1O1	1.423×10^5	0.9954	10.45	GT1O1	5.188×10^4	0.9694	1.389
	AT2O1	1.487×10^5	0.9903	11.41	GT2O1	5.517×10^4	0.9926	1.571
	AT1O2	1.294×10^5	0.9955	8.637	GT1O2	5.450×10^4	0.9878	1.533
40.0	BT1O1	8.582×10^4	0.9631	6.066	HT1O1	2.938×10^4	0.9860	0.446
	BT2O1	9.804×10^4	0.9779	4.962	HT2O1	3.159×10^4	0.9854	0.515

					HT1O2	3.288×10^4	0.9691	0.558
	CT1O1	7.924×10^4	0.9946	3.241	IT1O1	5.347×10^4	0.9804	1.476
31.5	CT2O1	8.514×10^4	0.9802	3.742	IT2O1	5.700×10^4	0.9965	1.677
					IT1O2	5.845×10^4	0.9638	1.763
	DT1O1	5.416×10^4	0.9842	1.514	KT1O1	6.643×10^4	0.9902	2.278
22.4	DT2O1	5.044×10^4	0.9888	1.313	KT2O1	6.700×10^4	0.9853	2.317
					KT1O2	7.237×10^4	0.9954	2.704

4 Contact damping ratio and theoretical correction

The contact damping ratios of the tested ballast grains can be obtained according to the widely used method. However, it is necessary to take account of the nonlinear characteristics of the ballast contact and the non-closure of the hysteresis curve due to residual strain. A modification to the method is proposed based on a simplified theoretical analysis, and the corresponding contact damping ratios of the ballast grains with different particle sizes are obtained. The derived theoretical correction formula for the damping ratio can also provide a reference for the research on contact damping of similar nonlinear systems considering plastic deformation.

4.1 Damping ratio correction for nonlinear stiffness system

To obtain the damping ratio, the method (iv) mentioned in the Introduction, based on the ratio of dissipated energy to stored energy, is a general method that is often used to study damping. For a conservative elastic body, an applied dynamic stress σ and the associated dynamic strain ε are coincident in time under a harmonic load. However, for a non-conservative elastic body, there is a lag between the application of the stress and the resulting strain. If the dynamic stress and strain are plotted against each other, a hysteresis loop is formed, as shown in Fig. 5 (in terms of force and deflection). As the load is applied, the curve passes from D through C to A; when the load is removed the curve does not return by the same path but passes through E. The point O is defined as the centre of the line AD between the highest and lowest points of the hysteresis loop.

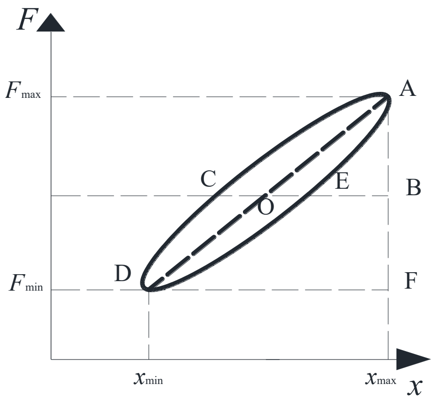

Fig. 5 Typical hysteresis loop for a system with linear stiffness, plotted in terms of force F and deflection x.

The hysteresis loops can be used to determine the damping ratio ζ, which can be expressed as

$$\zeta = S_{\mathrm{h}} / 4\pi S_{\mathrm{top}}, \tag{5}$$

where S_{h} is the area within the hysteresis loop DCAED, reflecting the energy dissipation during one loading cycle, and S_{top} is the area of the triangle △AOB, as shown in Fig. 5. The factor of 4 is introduced as the area of the triangle AOB is one quarter of the area of the triangle △ADF, corresponding to the maximum stored elastic strain energy in one cycle. Eq. (5) has been widely used in various fields to obtain the damping ratio [76-78].

The hysteresis loop for a linear stiffness system is centrosymmetric about the point O, as shown in Fig. 5. However, for a system with a nonlinear stiffness behaviour, the shape of the hysteresis loop is asymmetric, so the area of △AOB is no longer equal to one quarter of the maximum stored elastic strain energy.

To investigate this, numerical simulations have been performed using the ODE45 function of Matlab to determine the response of a nonlinear spring in parallel with a dashpot under forced vibration. For a typical hysteresis loop (Fig. 6), the areas of various triangles are calculated; these are identified as the top triangle, with area S_{top}, and the total triangle, with area S_{tot}. The strain energy calculated using each of these is then compared.

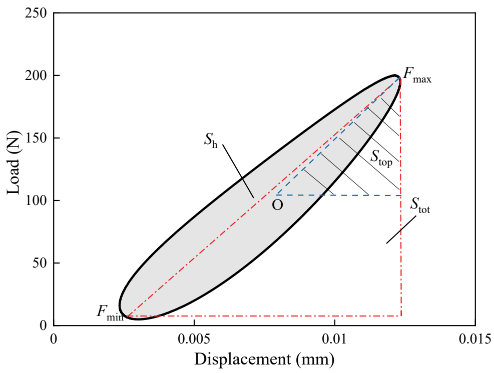

Fig. 6 The load-displacement curve of an example non-linear system

A nonlinear system is introduced with a stiffness behaviour that corresponds to a Hertzian law. For this nonlinear system, the dynamic equation is:

$$m\ddot{x}(t)+Gx(t)^{1.5}+c\dot{x}(t)=F_1+F_0\sin(\omega t), \qquad (6)$$

where m is the mass (kg), F_0 is the amplitude of the harmonic external load (N), F_1 is the average value of external load (N). G is the coefficient of force and displacement (N/m$^{1.5}$), and c is the damping coefficient (N·s/m).

Since the system has a nonlinear stiffness, the relationship between elastic force and displacement in the absence of damping is given by $F_k=Gx^{1.5}$, as shown in the blue curve of Fig. 7. Compared with this, the damped system forms a hysteresis loop on either side of the non-linear stiffness curve, shown by the red curve.

In practice, for a measured load-deflection behaviour the underlying theoretical elastic behaviour is unknown. Therefore, as an approximation to it, the average between the loading and unloading curves will be used, as also shown in Fig. 7. Two different methods are used to obtain the average between the loading and unloading curves. The first is to calculate the average value of the forces during loading and unloading that correspond to the same displacement. The second is to calculate the average value of the displacements corresponding to the same force. The area under the average curve based on equal displacements is termed S_{av_d}, the corresponding area for the average curve based on equal forces is S_{av_f}, and the area under the theoretical stiffness curve (which is used as a reference) is termed S_{st}.

Simulations have been carried out by numerical integration of the nonlinear system in Eq. (6) for different sets of input parameters A-1 to A-7, as listed in Table 3. These parameters are chosen to be typical of the ballast stones found in Section 3: the load frequency ω is 0.0644 rad/s, and the elastic force (in N) f = $4.5\times10^9\times x^{1.5}$, where x is the displacement in m. The mass in Eq. (6) is arbitrary but is given the value 0.170 kg. Fig. 8(a) and Table 3 show the calculated damping ratios obtained based on the different definitions of the area defining the elastic strain energy introduced above, as follows:

$\zeta_{top} = S_h/(4\pi S_{top})$ is based on the area of the top triangle (Fig. 6);

$\zeta_{tot} = S_h/(\pi S_{tot})$ is based on the area of the total triangle (Fig. 6);

$\zeta_{av\_d} = S_h/(\pi S_{av\_d})$ is based on the area under the average curve obtained for equal displacements (Fig. 7);

$\zeta_{av\_f} = S_h/(\pi S_{av\_f})$ is based on the area under the average curve obtained for equal forces (Fig. 7);

$\zeta_{st} = S_h/(\pi S_{st})$ is based on the area under the theoretical stiffness curve (Fig. 7), which corresponds to the actual stored energy in the nonlinear system and is used as the reference.

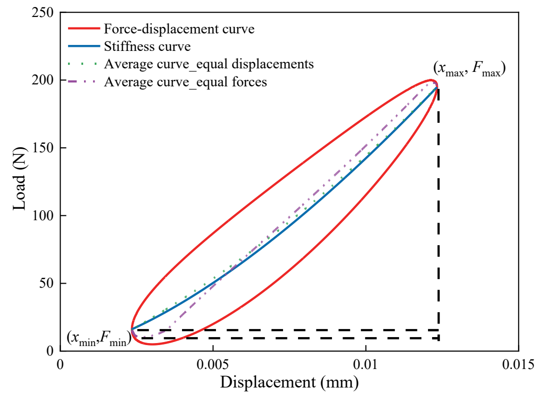

Fig. 7 The hysteresis loop of a non-linear system, and the average of loading and unloading curves and different stiffness curves

It can be seen from Fig. 8(a) and Table 3 that there are some differences in the values of the damping ratios ζ obtained using the areas of different regions to represent the strain energy. Specifically, using the area under the average curve gives a close approximation to the elastic behaviour over most of the load range. Moreover, Fig. 7 indicates that the curve obtained by averaging for the same displacements gives better agreement with the undamped stiffness curve than that obtained using the same forces. This is also reflected in the damping ratio results and is a consequence of the fact that the elastic force is proportional to the displacement, whereas the damping force is related to the velocity and therefore does not follow the displacement. Averaging the force for a given displacement can therefore cancel out the positive and negative acting damping forces. It can also be seen from Fig. 8(a) that the damping ratio calculated using the curve obtained by averaging for the same displacements, i.e., the purple downward triangles, is very close to the $y = x$ curve, which means that the corrected damping ratio is consistent with the theoretical damping ratio.

The relative errors in the values of the damping ratio ζ obtained using the area of different regions are shown in Fig. 8(b). These relative errors δ are calculated as:

$$\delta = \frac{\zeta_{\mathrm{cal}} - \zeta_{\mathrm{st}}}{\zeta_{\mathrm{st}}} \times 100\%, \tag{7}$$

where ζ_{cal} indicates the calculated damping ratio obtained by using different areas. The calculated damping ratio $\zeta_{\mathrm{av\_d}}$ obtained using the area under the average curve for equal displacements $S_{\mathrm{av\_d}}$ is closer to the reference damping ratio ζ_{st} than those obtained using the areas of the top triangle, or total triangle. So, it is reasonable to use the following equation to determine the damping ratio for a non-linear system:

$$\zeta_{\mathrm{av\_d}} = S_{\mathrm{h}} / (\pi S_{\mathrm{av\_d}}), \tag{8}$$

As shown in Fig. 8(b), the relative error of the calculated damping ratio obtained by Eq. (8) with respect to the reference damping ratio is close to 0, between -0.2% and -2.6%. By contrast, the damping ratio obtained by the traditional method, Eq. (5) has much larger relative errors, between 5.8% and -14%. This demonstrates the improved accuracy of the proposed in representing the strain energy in non-linear systems correction method compared with the traditional method.

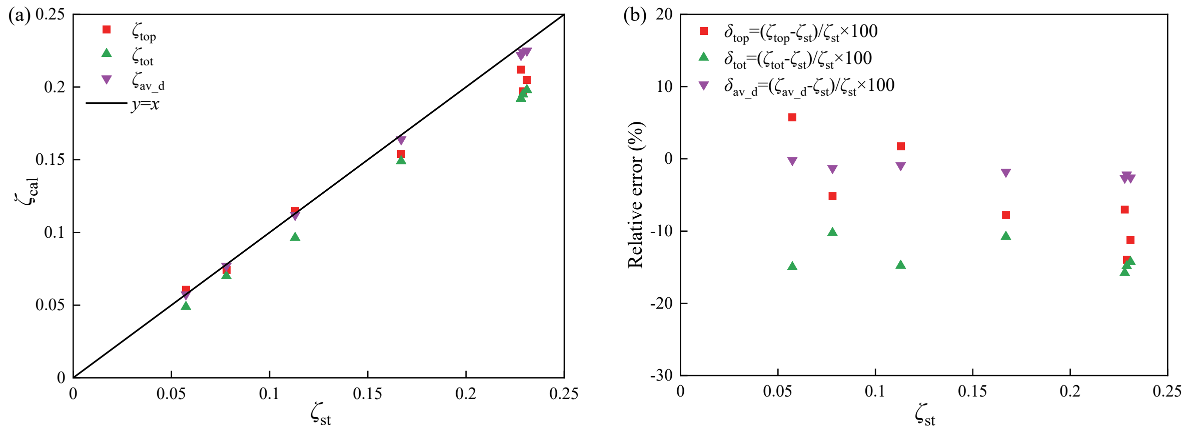

Fig. 8 The calculated damping ratios and corresponding relative errors obtained from simulations. (a) The damping ratios calculated using different regions to approximate the strain energy. (b) The relative errors of different estimates of the damping ratios calculated using different regions to approximate the strain energy.

Table 3. Calculated damping ratios obtained through numerical integration, using different areas to represent the strain energy

No.	F_{min} (N)	F_{max} (N)	c (kN·s/mm)	ζ_{top}	ζ_{tot}	ζ_{av_d}	ζ_{av_f}	ζ_{st}
A-1	5	200	112	0.197	0.195	0.224	0.208	0.229
A-2	2.5	200	109	0.212	0.192	0.222	0.207	0.228
A-3	10	200	115	0.205	0.198	0.225	0.211	0.231
A-4	5	200	106	0.154	0.149	0.164	0.162	0.167
A-5	5	200	52.9	0.115	0.0963	0.112	0.108	0.113
A-6	5	200	34.7	0.074	0.070	0.077	0.074	0.078
A-7	5	200	26.5	0.0607	0.0488	0.0573	0.0573	0.0574

4.2 Theoretical correction of damping ratio to allow for residual deformation

As noted in Section 2.2, the hysteresis loop is not usually closed owing to a small amount of settlement or plastic deformation after each load cycle [79, 12]. The damping ratios calculated using the method proposed in Section 4.1 will be affected by this, so in this section the effect of plastic deformation on the damping ratio is determined and a correction is introduced to the calculated results to allow for this.

To approximate the plastic deformation, a slowly varying monotonic function $p(t)$ is added to the response of the single-degree-of-freedom system, so the total displacement $x_n(t)$ including plastic deformation becomes $x_n(t)= x(t)+p(t)$, where $x(t)$ is the deflection in the time domain without plastic deformation.

First, a simple linear system is simulated, both with and without damping, and the force-displacement behaviour under harmonic loading is shown in Fig. 9, with and without plastic deformation. The parameters used to obtain the results in Fig. 9 are: stiffness k=1000 N/mm, mass m=0.01 kg, frequency of loading ω = 0.01 rad/s, and where damping is included a damping ratio of 0.2 is introduced. The load is set as F=102.5+97.5×sin (0.01×t) N, where t is the time in s; this load ranges from a minimum of 5 N to a maximum of 200 N. The red line OA represents the force-displacement curve of the system without plastic deformation, while the blue lines OB-BC represent that with plastic deformation and the black dotted line BM is the average curve between the loading and unloading lines. The degree of non-closure due to plastic deformation is given by $d_p = p(T)$, that is, the distance of segment OC in Fig. 9(a), where $T = 2\pi/\omega$ is the period of one cycle. This can be compared with the peak-to-trough displacement amplitude d_m, that is, the distance of segment OD in Fig. 9(a), which in this case is 0.195 mm.

It can be seen from Fig. 9 that the presence of plastic deformation and damping have different influences on the shape of the load-displacement curve. By comparing the solid curves of Fig. 9(a) and (b), it can be seen that due to the presence of damping, the force-displacement curve of cyclic loading and unloading forms a closed hysteresis curve. By comparing the red and blue curves in Fig. 9(a), it can be seen that, with residual strain, the unloading curve cannot return to the initial position after the unloading stage; the plastic deformation leads to the non-closure of the hysteresis curve. By comparing the red curve in Fig. 9(a) with the blue curve in Fig. 9(b), it is clear that the presence of damping and plastic deformation has a superimposed effect on the curve.

From the simulated response curves, the equivalent damping ratios are calculated using the method presented in Section 4.1, i.e. using the ratio of the area of the hysteresis loop to the area under the curve formed by the average of the loading and unloading curves. For the cases in which the damping is set to 0, this gives an estimate of the equivalent damping ratio representing plastic deformation, whereas for the damped spring it gives an estimate of the combined damping effect. The results for different amounts of plastic deformation d_p are listed in Table 4. It can be seen from Table 4 that the differences between the calculated damping ratios for the cases with and without damping are all around 0.1, which corresponds to the given damping ratio of 0.1 introduced in the model. In some of these cases the equivalent damping ratio due to plastic deformation becomes quite large compared with the given damping.

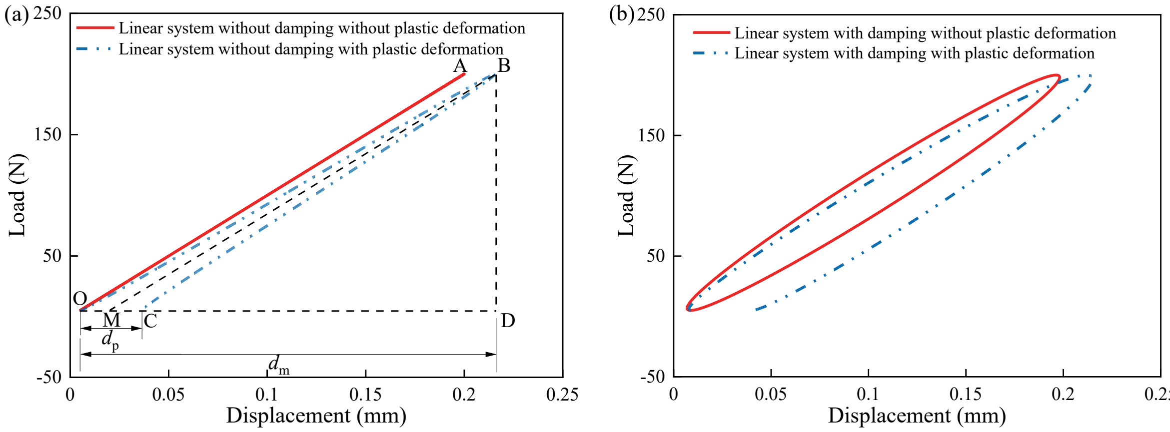

Fig. 9 Force-displacement curves for the undamped and damped linear systems with and without plastic deformation. (a) Undamped linear system. (b) Damped linear system.

Table 4. Simulation results of damping ratios obtained for linear system with different amounts of plastic deformation, without and with damping

	d_p (mm)	ζ	S_h (N·mm)	S_{av_d} (N·mm)	ζ_{av_d}	$\Delta\zeta$
Without damping	0	0	0	15.032	0	
	0.006	0	0.613	19.000	0.010	
	0.032	0	3.063	18.918	0.051	
	0.063	0	6.126	18.639	0.102	
	0.303	0	30.631	12.874	0.757	
With damping	0.000	0.1	5.743	18.512	0.099	0.099
	0.006	0.1	6.357	18.655	0.108	0.098
	0.031	0.1	8.805	18.624	0.149	0.098
	0.062	0.1	11.868	18.417	0.199	0.096
	0.302	0.1	36.372	13.525	0.856	0.099

It is clear that the presence of plastic deformation can have a significant effect on the calculation of the damping ratio. In the experiments, the effect of plastic deformation should be removed from the results to obtain the damping ratio caused by the damping itself. It can be seen from the above analysis, that this can be achieved by subtracting the damping ratio produced by plastic deformation from the total damping ratio. However, for the experiments, the damping ratio produced by plastic deformation is difficult to obtain directly. A method for estimating the increment in damping ratio due to plastic deformation $\Delta\zeta$ is required.

For this it is assumed that the plastic deformation occurs gradually during the cycle, as indicated in Fig. 9(a).

It can be seen from Fig. 9(a) for an undamped linear system that the damping ratio with plastic deformation ζ_{with} could be obtained by:

$$\zeta_{\text{with}} = \frac{S_{\text{OBC}}}{S_{\text{MBD}} \times \pi} = \frac{d_{\text{p}} \times (F_{\max} - F_{\min})}{(d_{\text{m}} - d_{\text{p}}/2) \times (F_{\max} - F_{\min}) \times \pi} = \frac{d_{\text{p}}}{(d_{\text{m}} - d_{\text{p}}/2) \times \pi}, \tag{9}$$

where $F_{\min}$ and $F_{\max}$ are the minimum and maximum loads, and d_{m} and d_{p} are the displacements shown in Fig. 9(a).

In this case, the damping ratio without plastic deformation ζ_{without}=0, so the increment of damping ratio $\Delta\zeta$ due to plastic deformation can be obtained from $\Delta\zeta=\zeta_{\text{with}}-\zeta_{\text{without}}= d_{\text{p}}/((d_{\text{m}}-d_{\text{p}}/2)\times\pi)$. From this, the corrected damping ratio ζ_{cor} can be obtained by:

$$\zeta_{\text{cor}} = \zeta_{\text{av\_d}} - \Delta\zeta = \zeta_{\text{av\_d}} - d_{\text{p}}/((d_{\text{m}}-d_{\text{p}}/2)\times\pi), \tag{10}$$

To verify whether this expression is appropriate to estimate the damping ratio difference for other cases, and considering that the contact behaviour of ballast grains is nonlinear Hertzian contact, a nonlinear stiffness is introduced in the simulations to represent the material and stiffness properties of ballast particles to analyse the influence of residual strain on the damping ratio estimates. Fig. 10(a) shows the simulation results in terms of the hysteresis loop. In the simulations, the parameters identified as A-4 in Table 3 are used and a plastic deformation is introduced. For comparison, the measured results are shown in Fig. 10(b) for the second loading cycle of ballast sample A. By setting a reasonable degree of plastic deformation, the hysteresis loop obtained from the simulations is similar to the measured results.

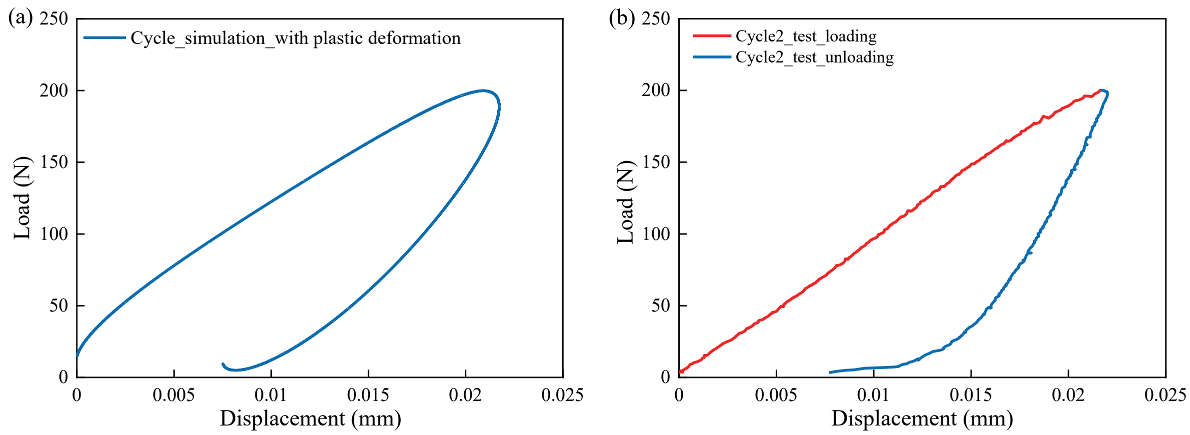

Fig. 10 Example comparison of simulated and measured hysteresis loops. (a) Simulated hysteresis loop. (b) Measured hysteresis loop (cycle 2 of ballast sample A).

Table 5 shows simulation results obtained with different amounts of plastic deformation based on the nonlinear system. These results were obtained using the parameters from the tested ballast grain pairing A, setting the same values of $d_{\text{p}}/d_{\text{m}}$ as found in the test results. The damping ratios were calculated using the average of the loading and unloading curves determined using values with the same displacement or values with the same force (see Fig. 7). In Fig. 11 the damping ratio difference $\Delta\zeta$ is plotted against the estimate

$$\Delta\zeta_{est}=d_p/((d_m-d_p/2)\times\pi), \tag{11}$$

for results calculated with different given damping ratios and different degrees of plastic deformation. These results are again determined from the simulations based on the average stiffness curves obtained for equal displacement or equal force. Using the stiffness curves based on equal displacements or equal forces gives similar results when the degree of plastic deformation is small; however, when the amount of plastic deformation is large, the results are more reasonable when based on the equal force stiffness curve. This is because the curve based on equal forces is closer to the actual stiffness curve when the degree of non-closure of the hysteresis loop is larger.

It can be seen from Fig. 11 that $\Delta\zeta_{est}$ is an appropriate estimator for the damping ratio difference, with a regression coefficient R^2=0.98. For values of $\Delta\zeta_{est}$ less than 0.2, using the average stiffness curve based on equal displacements is suitable to predict the damping ratio difference; for this region the deviation between $\Delta\zeta_{est}$ and damping ratio difference $\Delta\zeta$ is less than around 10%. Thus this expression could be used as a correction to the damping ratio to allow for plastic deformation in the experimental results, at least when the degree of non-closure corresponding damping ratio is less than 0.2. If the degree of non-closure is larger than this, the estimate of damping is likely to become unreliable so it is recommended not to apply a correction.

Table 5. Numerical calculation results of damping ratios with different plastic deformation (with and without plastic deformation, with some parameters of ballast A)

Given damping ratio	d_p/d_m of test results	Plastic deformation (d_p) mm	Max deformation (d_m) mm	Using equal displacements			Using equal forces			$\Delta\zeta_{est} = d_p/((d_m-d_p/2)\times\pi)$
				$\zeta_{without}$	ζ_{with}	Damping ratio difference $\Delta\zeta$	$\zeta_{without}$	ζ_{with}	Damping ratio difference $\Delta\zeta$	
	0.894	0.179	0.200		0.997	0.784		0.655	0.456	0.515
	0.350	0.042	0.120		0.349	0.136		0.327	0.128	0.135
	0.328	0.039	0.119		0.337	0.124		0.318	0.119	0.125
0.2	0.097	0.010	0.105	0.213	0.231	0.018	0.199	0.229	0.030	0.032
	0.380	0.047	0.123		0.368	0.155		0.341	0.142	0.149
	0.133	0.014	0.106		0.245	0.032		0.241	0.042	0.045
	0.026	0.003	0.101		0.221	0.008		0.205	0.006	0.008

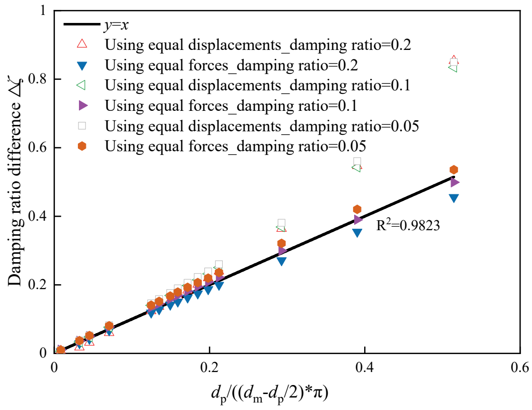

Fig. 11 The relationship between the increase in damping ratio due to plastic deformation and the parameter $\Delta\zeta_{est} = d_p/((d_m-d_p/2)\times\pi)$.

4.3 Application to measured results

Using the damping ratio calculation and correction formulas derived in Sections 4.1 and 4.2, the load-displacement results from 21 experiments were analyzed. The damping ratios of the eight ballast grain pairs, before and after plastic strain correction, together with their differences, are shown in Fig. 12 - Fig. 14. These results present representative and demonstrative case studies to illustrate the applicability of the proposed correction method to ballast grains with specific geometries and particle sizes. In addition, when conducting DEM simulations of ballast particles with the same particle size as in this experiment, the damping ratio obtained in this section can be used as the corresponding input parameter. However, it should be emphasized that parameter selection must be made with caution, as the experimental results reported herein are derived under specific cyclic loading conditions and particle geometries. Nonetheless, the damping ratio calculation method proposed in this study, developed from uniaxial compression tests, offers a new framework for researchers seeking to directly determine the contact parameters of ballast. If necessary, corresponding studies can be conducted according to the proposed method for the specific research object. The damping ratios of the tested ballast grains in the initial orientation derived using Eq. (8) for each cycle, without allowing for residual deformation, are shown in Fig. 12. For both fresh and used ballast, the apparent damping ratio decreases rapidly over the first five cycles, especially the first two, and then stabilises over the next five cycles due to the influence of residual deformation. The used ballast tends to reach stable behaviour more quickly. This may be because, as a result of previous loading, the surface of the used ballast has become more polished so that there is less breakage of small asperities. It can also be seen that the damping ratios obtained for fresh ballast are greater than for used ballast with the same particle size.

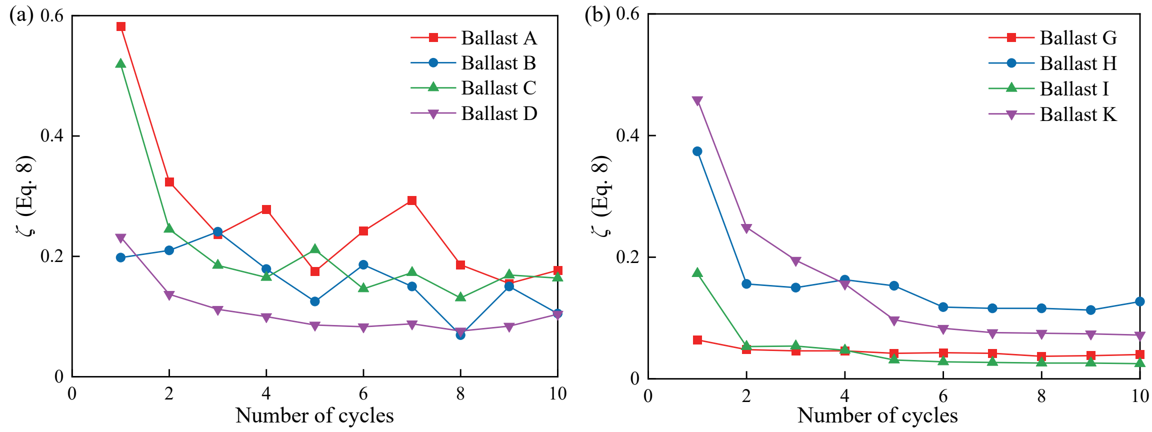

Fig. 12 Damping ratios ζ of tested ballast particles from each loading cycle obtained using Eq. (8). (a) Fresh ballast particles. (b) Used ballast particles.

Applying the correction in Eq. (10) to the measured hysteresis loops, Fig. 13 shows the damping ratio differences (i.e. the damping corresponding to plastic deformation) of all test ballast particles in the initial orientation. In general, the values of damping ratio difference of the first cycles are quite large but in subsequent cycles they become smaller.

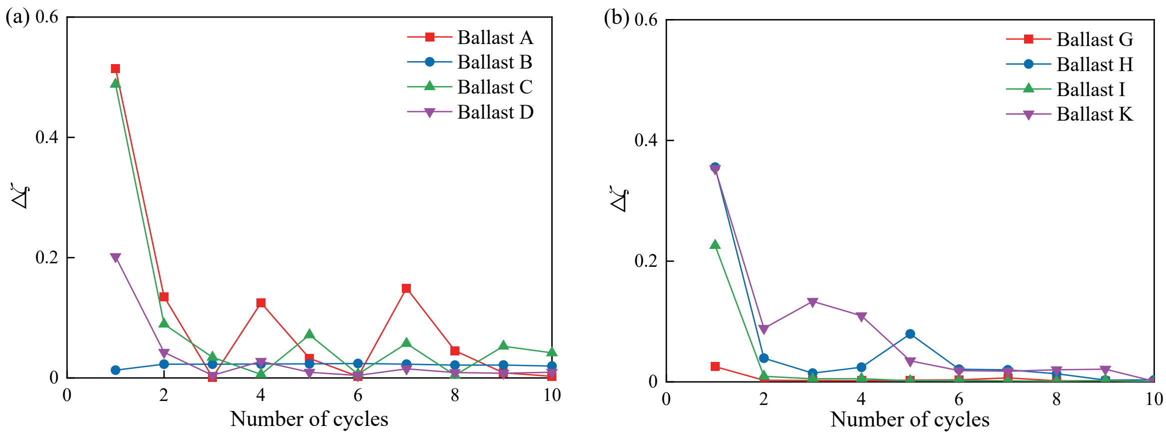

Fig. 13 Damping ratio differences $\Delta\zeta$ due to residual deformation at each cycle. (a) Fresh ballast. (b) Used ballast.

The corrected damping ratios ζ_{cor} of the tested ballast particles from each cycle in the initial orientation are shown in Fig. 14. Table 6 shows the average corrected damping ratios from the last five cycles of all tested ballast particles, as well as the standard deviation of ζ_{cor} and the uncorrected damping ratio ζ_{av_d}. The small values of the standard deviation reflect the stability off the damping ratio within the last five cycles of loading.

It can be seen from Table 6 and Fig. 14 that the values of the corrected damping ratios are smaller than the uncorrected ones shown in Fig. 12, with a more stable trend for most of the cycles. In addition, the standard deviations of all ballast pairs are reduced by introducing the correction. The corrected damping ratios of the fresh ballast particles are generally greater than those of the used ballast particles with the corresponding particle size. The same pair of ballast demonstrates good consistency across different test groups, with only limited variations attributable to the nonlinear nature of the ballast contact surfaces. In comparison with previously reported results (ranging from 0.01 to 0.8 [34, 40, 56-63]), the damping ratios of the tested ballast are within a reasonable range. In addition, to validate the effectiveness of the proposed damping ratio correction method, a DEM simulation of the uniaxial compression test on ballast pair A was performed, and the resulting displacement curves under cyclic loading and unloading were compared with the experimental data (see Appendix B).

It should also be noted that, although it is found that the initial load/unload responses of the same particle under different orientations exhibit noticeable variability, the stable parameters show much less variation. Specifically, the nonlinear stiffness obtained from the ninth cycle (Table 2) and the average damping loss factor calculated over the last five cycles (Table 6) both present relatively small scatter. The average coefficient of variation is approximately 4% for the nonlinear stiffness and 8% for damping. This suggests that while the early cycles are significantly affected by orientation-dependent contact geometry, surface roughness, and the initiation of local damage, the subsequent cycles lead to a stabilized response. Therefore, the converged values provide more robust and repeatable indicators of the particle-scale mechanical behavior.

Table 6. Corrected damping ratios ζ_{cor} and uncorrected values ζ of tested ballast grains and the standard deviation over the last five cycles

	Uncorrected values		**Corrected values**		
Ballast	Average ζ (Eq. (8))	Standard deviation of ζ	Average ζ_{cor} (Eq. (10))	Average ζ_{cor} of all tests	Standard deviation of ζ_{cor}
AT1O1	0.211	0.183	0.168		0.051
AT2O1	0.177	0.016	0.166	0.165	0.011
AT1O2	0.199	0.055	0.161		0.016
BT1O1	0.132	0.049	0.110	0.119	0.040
BT2O1	0.134	0.024	0.127		0.022
CT1O1	0.156	0.152	0.124	0.136	0.021
CT2O1	0.175	0.043	0.147		0.032
DT1O1	0.087	0.044	0.078	0.074	0.013

DT2O1	0.073	0.031	0.069		0.030
GT1O1	0.040	0.011	0.037		0.005
GT2O1	0.032	0.019	0.030	0.037	0.019
GT1O2	0.048	0.027	0.043		0.018
HT1O1	0.118	0.027	0.106		0.018
HT2O1	0.139	0.082	0.090	0.095	0.021
HT1O2	0.098	0.051	0.089		0.030
IT1O1	0.026	0.046	0.025		0.017
IT2O1	0.022	0.010	0.020	0.024	0.009
IT1O2	0.031	0.005	0.028		0.002
KT1O1	0.076	0.145	0.060		0.052
KT2O1	0.089	0.075	0.071	0.065	0.051
KT1O2	0.066	0.011	0.064		0.010

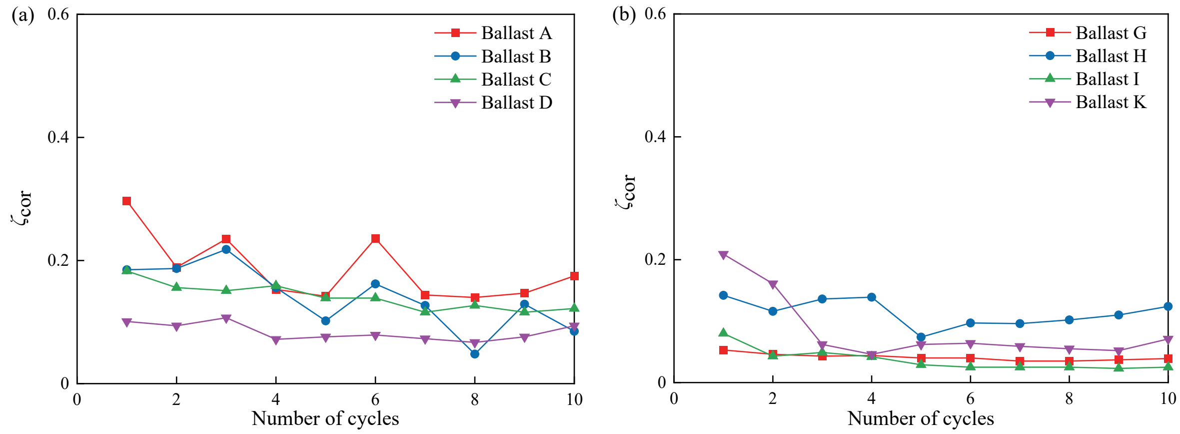

Fig. 14 The corrected damping ratios ζ_{cor}. (a) Corrected damping ratio (Eq. (10)) of fresh ballast particles at each cycle. (b) Corrected damping ratio (Eq. (10)) of used ballast particles at each cycle.

5 Conclusions

The macroscopic dynamic behaviour of ballasted track composed of ballast particles is closely related to the mesoscopic contact characteristics between the ballast particles, such as the contact stiffness and contact damping. Based on uniaxial compression tests, the hysteresis curves of eight pairs of ballast grains have been obtained, covering a typical range of particle sizes and service states. Theoretical analysis has been used to propose modified formulas for the contact damping ratio applicable to a system with nonlinear stiffness behaviour and to correct for the presence of plastic deformation. From these measurements and modified formulas, the contact stiffness and damping characteristics of the ballast grains were investigated. The following conclusions can be drawn.

- For the specific load range considered (5 N to 200 N), the contact behaviour between the ballast stones approximately obeys a Hertzian nonlinear stiffness. Owing to the uneven surface of the fresh ballast grains, their effective radii and nonlinear contact stiffness are mostly greater than those of used ballast grains. For the fresh ballast samples the nonlinear stiffness values are between 5.4×10^4 N/mm$^{1.5}$ and 1.4×10^5 N/mm$^{1.5}$, while the values for used ballast are lower, between 2.9×10^4 N/mm$^{1.5}$ and 6.6×10^4 N/mm$^{1.5}$.
- A revised calculation method for the contact damping ratio of a non-linear system is proposed, which uses the area under the average of the loading and unloading curves for equal displacements to represent the strain energy. Simulation results demonstrated that this method gives a better accuracy. On this basis, the differences in apparent damping ratio caused by plastic deformation can be estimated from the degree of non-closure due to plastic deformation, and the calculated damping ratios can be corrected by this damping ratio difference.
- After applying the correction for plastic deformation, the average damping ratios of fresh ballast samples are between 0.078 and 0.168, while the values of used ballast particles are between 0.025 and 0.106. These values are smaller than before applying the correction and have a smaller standard deviation.

It should be noted that 21 measurements based on eight pairs of granite ballast grains were analysed in this study, covering a representative range of particle sizes of fresh and used ballast. Future work could further improve the independence and representativeness of the results by increasing the number of fully independent particle pairs tested, which would also help improve statistical reliability and establish more generalizable conclusions. Although consistent nonlinear Hertzian-type responses confirm method robustness to some extent, the repeatability was constrained by surface wear after the initial orientation cycle. Future studies should investigate repeatability across multiple particles to assess variability and uncertainty. Tests were limited to 10 cycles, during which damping stabilization was observed, providing insight into short-term responses and establishing testing principles, though long-term degradation is not captured. This paper establishes the testing principles, with test numbers expandable as needed. Future work will extend to larger cycles to better reflect in-service ballast conditions.

While ballast mineralogy affects contact characteristics, particle size and shape are not expected to substantially influence surface properties. The proposed methods for estimating contact stiffness and damping ratio provide a practical framework for analyzing individual grain contacts under controlled conditions. Although the method's theoretical basis supports broader applicability, it has been demonstrated on a limited range of geometries; future work should include diverse morphologies, mineralogies, and sensitivity analyses. The parameters obtained are specific to the tested ballast size and loading regime and cannot be directly generalized to other types or operational scenarios. Therefore, caution is advised when selecting DEM simulation parameters based on these results, and further testing is required to extend the applicability of the proposed approach to a broader range of conditions. Focusing solely on stiffness and damping simplifies true contact mechanics, which also involve friction, surface degradation, time-dependent plasticity, and rotational resistance. Localized plasticity was quantified via an equivalent damping ratio, but the small sample size and limited cycles restrict representativeness. Variations over time are not fully covered, though differences between fresh and used ballast were captured. Future studies could directly characterize local contact geometry, such as radii of curvature and surface roughness, and track the evolution of damage during the cycles using techniques such as digital image correlation, microscope or micro-CT. Combining these approaches with microscopic analysis of asperity deformation and microcracks will enable a more comprehensive understanding of ballast contact behavior and provide deeper mechanistic insight into the role of particle-scale heterogeneity in long-term performance.

Acknowledgments

This work was supported by the UK EPSRC (Grant No. EP/M025276, Track to the Future), the National Natural Science Foundation of China (No. 12302019; No. 12393781) and the International Exchange Program for Graduate Students, Tongji University.

Appendix A

Table A1 Calibration tests, contact models and parameters used in DEM models of railway ballast

Author	Calibration test	Contact model	Normal stiffness (MN/m)	Shear stiffness (MN/m)	Friction coefficient	Local damping	Normal/Shear damping ratio
Laryea [32]	Box test	Linear	0.6	0.6	0.6	/	/
Indraratna [33]	Direct shear test	Linear	52	52	0.8	/	/
Zhang [34]	Cyclic loading test	Linear	15	10	0.5	/	0.15
Lu [35]	Box test	Linear	100	100	0.3	/	/
Lim [36]	Box test	Linear	2000	2000	0.5	/	/

McDowell [37]	Triaxial test	Linear	1000	1000	0.5	/	/
Jia [38]	Lateral resistance test of ballast box	Linear	20	20	0.5	0.7	/
Xiao [39]	Field driving test	Linear	50	50	0.55	/	/
Fu [40]	Cyclic loading test model test	Linear	10	10	0.7	0.3	0.2
Xiao [41]	Triaxial test	Linear	18.2	16	0.65	0.03	/

Author	Calibration test	Contact model	Shear/Elastic modulus (GPa)	Poisson's ratio	Friction coefficient	Local damping	Normal/shear damping ratio
Li [42]	Box test	Hertz	28	0.25	0.5	0.7	/
Coop [43]	Triaxial test	Hertz	70	0.25	0.6-0.8	/	/
Yang [44]	Cyclic loading test	Hertz	10	0.25	0.86	0.7	/
Chi [45]	Field static and dynamic tests	Hertz	25	0.18	0.6		
Ahmed [25]	Triaxial test	Hertz	1.0	/	0.84	0.05	/

Author	Calibration test	Contact model	Young's modulus (GPa)	Poisson's ratio	Friction coefficient	Radius	Compressive strength (MPa)
Suhr [46]	Compression and direct shear tests	CDM	50/67/85	0.3	0.4/0.5	/	50/100/150/ 200/250
Harkness [47]	Triaxial test	CDM	5	0.2	0.53	4 mm	200
Suhr [48]	Compression and direct shear tests	CDM	60/30	0.2	0.45	0.0154/ 0.0098	600/280

Author	Calibration test	Contact model	Normal stiffness (MN/m)	Shear stiffness (MN/m)	Friction coefficient	Local damping	Normal/shear damping ratio
Guo [49]	Direct shear test	RRLM	0.4/1/10/100	0.4/1/10/1 00	0.5	0.9	/
Li [50]	In situ impact test	RRLM	500	500	0.7	0.05	/

Appendix B

Considering that one of the main objectives of this study is to derive representative ballast contact parameters using the proposed computational method to serve as a reference for DEM simulations, the experimentally obtained parameters were employed to conduct a discrete element simulation of a ballast pair under uniaxial compression. The purpose was to verify whether the derived parameters can reliably reproduce the mechanical behavior between ballast particles. Specifically, the contact damping ratio identified in Section 4.3, together with the nonlinear Hertzian contact model and its associated parameters described in Section 3.2, were used to establish a uniaxial compression test model of ballast under cyclic loading, as illustrated in Fig. B1(a). In this model, the ballast pair was generated based on the actual geometry of ballast pair A. Consistent with the experimental setup, an initial load of 0-5 N was first applied, and the load was maintained at 5 N for 30 s to ensure stability. Subsequently, a cyclic load ranging from 5 to 200 N was imposed on the upper ballast particle, while lateral displacements were constrained to simulate the connection between the ballast and the supporting frame. The vertical displacement of the ballast was then extracted and compared with the experimental measurements, as shown in Fig. B1(b). It is worth noting that the damping ratio parameter input to the model corresponded to the average value of the last five experimental cycles (0.165). Accordingly, the comparison between experiment and simulation should primarily focus on the displacement responses in these last five cycles.

As shown in the Fig. B1, the simulated ballast displacement under uniaxial compression using the experimentally derived contact parameters agrees closely with the measured results. Both exhibit a sharp increase in displacement at the initial stage of loading, followed by cyclic fluctuations corresponding to the loading/unloading process, with the amplitude of these fluctuations gradually diminishing as the contacts stabilize. A slight discrepancy in displacement amplitude is observed in the early loading stage, which can be attributed to the use of damping ratio parameters obtained from the stabilized stage. In the last few loading cycles, the displacement amplitudes show good consistency. These results indicate that the experimentally derived contact parameters are capable of reliably characterizing the contact stiffness and damping behavior of ballast. Future research will focus on conducting more tests on the ballast particles to determine their contact parameters, as well as performing tests on ballast assemblies, such as box tests, in combination with simulations to further assess and validate the effectiveness of the method.

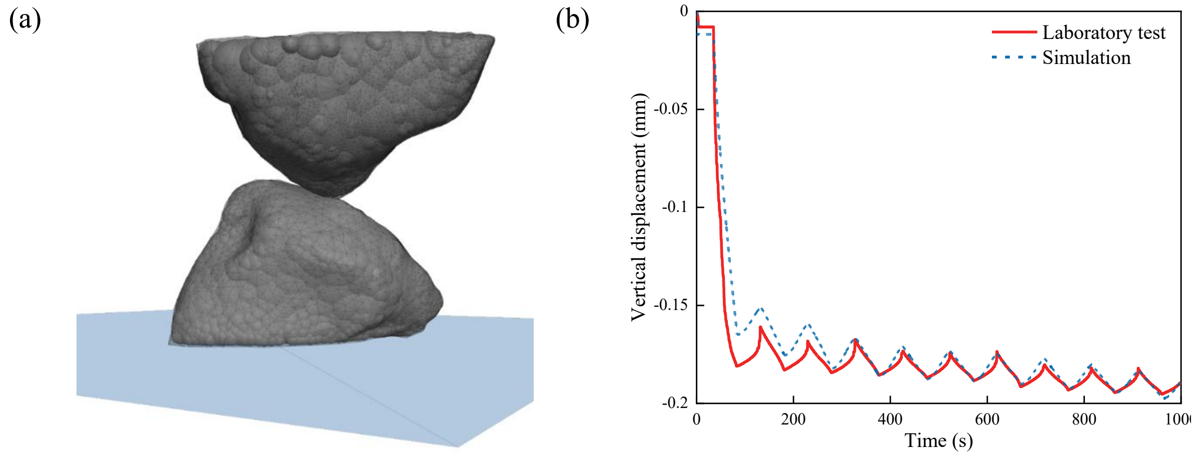

Fig. B1 DEM simulation of uniaxial compression and comparison with experimental ballast displacement. (a) DEM model; (b) Comparison of vertical displacement.

References

[1] Charoenwong C, Connolly DP, Colaço A, et al. Railway slab vs ballasted track: a comparison of track geometry degradation. Construction and Building Materials, 2023, 378:131121.

[2] Wu Y, Fu H, Bian X. Comparative study on dynamic responses of ballasted and ballastless tracks at critical velocity. Transportation Geotechnics, 2024, 48: 101354.

[3] Abadi T, Madhusudhan BN, Li H, et al. Reusing life-expired railway ballast: laboratory testing, shape analysis, and petrographic evaluation. Journal of Geotechnical and Geoenvironmental Engineering, 2023, 149(1): 04022123.

[4] Oregui M, Li Z, Dollevoet, R. An investigation into the modeling of railway fastening. International Journal of Mechanical Sciences, 2015, 92: 1-11.

[5] Chen C, Li PY, McDowell G, et al. Numerical study on ballast disturbance and maintenance performance of tamping and stone-blowing. Construction and Building Materials, 2025, 460: 139837.

[6] Zhang T, Zhou L, Luo Y. Energy evolution characteristics of ballasted track with elastic layers. Construction and Building Materials, 2024, 456: 139149.

[7] Xiao H, Ling X, Wang M, et al. Mechanical behaviour and energy evolution of polyurethane-mixed ballast under revised bonding constitutive model. Construction and Building Materials, 2022, 320: 126260.

[8] Zhang T, Zhou J, Luo Y, et al. Energy evolution characteristics of ballast particles and contact parameter study. International Journal of Mechanical Sciences, 2025: 110227.

[9] Suhr B, Butcher TA, Lewis R, et al. Friction and wear in railway ballast stone interfaces. Tribology International, 2020, 151: 106498.

[10] Deiros Quintanilla I, Combe G, Emeriault F, et al. X-ray CT analysis of the evolution of ballast grain morphology along a Micro-Deval test: key role of the asperity scale. Granular Matter, 2019, 21(2): 30.

[11] Ouhbi N, Voivret C, Perrin G, et al. 3D particle shape modelling and optimization through proper orthogonal decomposition: application to railway ballast. Granular Matter, 2017, 19(4): 86.

[12] Kamrin K. Nonlinear elasto-plastic model for dense granular flow. International Journal of Plasticity, 2010, 26(2): 167-188.

[13] Fu L, Zhou S, Guo P, et al. Dynamic characteristics of multiscale longitudinal stress and particle rotation in ballast track under vertical cyclic loads. Acta Geotechnica, 2021, 16(5): 1527-1545.

[14] Shi C, Fan Z, Connolly DP, et al. Railway ballast performance: recent advances in the understanding of geometry, distribution and degradation. Transportation Geotechnics, 2023, 41: 101042.

[15] Tan P, Xiao Y, Jiang Y, et al. Investigating influencing mechanisms of under-sleeper pads on lateral resistance of ballasted railway trackbed via hybrid DEM-FDM simulations. Transportation Geotechnics, 2024, 45: 101200.

[16] Cui X, Xiao H, Xu Y, et al. Discrete element analysis of the dynamic behavior of ballast track-subgrade system under train dynamic load. Soil Dynamics and Earthquake Engineering, 2024, 183: 108820.

[17] Setiawan DM. Advancing asphaltic rail tracks: Bridging knowledge gaps and challenges for sustainable railway infrastructure. Journal of the Mechanical Behavior of Materials, 2025, 34(1): 20250043.

[18] Chen J, Indraratna B, Ngo T. Assessing the Macro to Micro Properties of Recycled Ballast Mixtures by DEM Analyses for Enhanced Railroad Engineering. Journal of Geotechnical and Geoenvironmental Engineering, 2025, 151(6): 04025046.

[19] Kumar N, Suhr B, Marschnig S, et al. Micro-mechanical investigation of railway ballast behavior under cyclic loading in a box test using DEM: effects of elastic layers and ballast types. Granular Matter, 2019, 21(4): 106.

[20] Gao L, Shi S, Zhong Y, et al. Real-time evaluation of mechanical qualities of ballast bed in railway tamping maintenance. International Journal of Mechanical Sciences, 2023, 248: 108192.

[21] Brzeziński K, Gladky A. Clump breakage algorithm for DEM simulation of crushable aggregates. Tribology International, 2022, 73:107661.

[22] Suhr B, Six K. Simple particle shapes for DEM simulations of railway ballast: influence of shape descriptors on packing behaviour. Granular Matter, 2020, 22: 1-17.

[23] Wiącek J, Parafiniuk P, Molenda M, et al. DEM study of microstructural effects in friction of wheat on

corrugated steel surface. Tribology International, 2023, 183: 108435.
[24] Li C, Zhou X. Visualization of stick-slip shear failure process of granite by 3D reconstruction technique and DEM. Tribology International, 2022, 176: 107923.
[25] Ahmed S, Harkness J, Le Pen L, et al. Numerical modelling of railway ballast at the particle scale. International Journal for Numerical and Analytical Methods in Geomechanics, 2016, 40(5): 713-737.
[26] Aela P, Zong L, Yin ZY, et al. Calibration method for discrete element modeling of ballast particles. Computational Particle Mechanics, 2023, 10(3): 481-93.
[27] Suhr B, Six K. Efficient DEM simulations of railway ballast using simple particle shapes. Granular matter, 2022, 24(4): 114.
[28] Ngo T, Indraratna B. Analysis of deformation and degradation of fouled ballast: Experimental testing and DEM modeling. International Journal of Geomechanics, 2020, 20(9): 06020020.
[29] Danesh A, Mirghasemi AA, Palassi M. Evaluation of particle shape on direct shear mechanical behavior of ballast assembly using discrete element method (DEM). Transportation Geotechnics, 2020, 23: 100357.
[30] Alabbasi Y, Hussein M. Geomechanical modelling of railroad ballast: a review. Archives of Computational Methods in Engineering, 2021, 28(3): 815-39.
[31] Wong CP, Coop MR. Development of inter-particle friction in a railway ballast. Géotechnique Letters, 2020, 10(4): 535-41.
[32] Laryea S, Baghsorkhi MS, Ferellec JF, et al. Comparison of performance of concrete and steel sleepers using experimental and discrete element methods. Transportation Geotechnics, 2014, 1(4): 225-240.
[33] Indraratna B, Nimbalkar SS, Ngo NT, et al. Performance improvement of rail track substructure using artificial inclusions-Experimental and numerical studies. Transportation Geotechnics, 2016, 8: 69-85.
[34] Zhang X, Zhao C, Zhai W. Importance of load frequency in applying cyclic loads to investigate ballast deformation under high-speed train loads. Soil dynamics and earthquake engineering, 2019, 120: 28-38.
[35] Lu M, McDowell G. Discrete element modelling of ballast abrasion. Géotechnique, 2006, 56(9):651-655.
[36] Lim WL, McDowell GR. Discrete element modelling of railway ballast. Granular Matter, 2005, 7: 19-29.
[37] McDowell GR, Li H. Discrete element modelling of scaled railway ballast under triaxial conditions.

Granular matter, 2016, 18(3): 66.
[38] Jia W, Markine V, Guo Y. Efficiency analysis and optimisation of DEM for railway ballast track simulations: Multi-layer shape model of lateral resistance. Transportation Geotechnics, 2023, 40: 100977.
[39] Xiao H, Zhang Z, Chi Y, et al. Experimental study and discrete element analysis on dynamic mechanical behaviour of railway ballast bed in windblown sand areas. Construction and Building Materials, 2021, 304: 124669.
[40] Fu L, Zheng Y, Tian Z, et al. Importance of examining particle movements in modelling ballast bed via discrete element method. International Journal of Rail Transportation, 2022, 10(5): 547-561.
[41] Xiao J, Xue L, Zhang D, et al. Coupled DEM-FEM methods for analyzing contact stress between railway ballast and subgrade considering real particle shape characteristic. Computers and Geotechnics, 2023, 155: 105192.
[42] Li H, McDowell GR. Discrete element modelling of under sleeper pads using a box test. Granular Matter, 2018, 20(2): 26.
[43] Coop MR, Altuhafi FN, Wong CP. The discrete and continuum behaviour of railway ballast. Transportation Geotechnics, 2024, 46: 101251.
[44] Yang X, Yu L, Wang X, et al. Analysis of mesoscopic mechanical dynamic characteristics of ballast bed with under sleeper pads. Railway Engineering Science, 2024, 32(1): 107-123.
[45] Chi Y, Xiao H, Zhang Z, et al. Field experiment and numerical simulation investigation on the mechanical properties of ballast bed with elastic sleepers. Construction and Building Materials, 2023, 397: 132361.
[46] Suhr B, Skipper WA, Lewis R, et al. DEM modelling of railway ballast using the Conical Damage Model: a comprehensive parametrisation strategy. Granular Matter, 2022, 24(1): 40.
[47] Harkness J, Zervos A, Le Pen L, et al. Discrete element simulation of railway ballast: modelling cell pressure effects in triaxial tests. Granular Matter, 2016, 18: 1-13.
[48] Suhr B, Marschnig S, Six K. Comparison of two different types of railway ballast in compression and direct shear tests: experimental results and DEM model validation. Granular matter, 2018, 20(4): 70.
[49] Guo Y, Zhao C, Markine V, et al. Discrete element modelling of railway ballast performance considering particle shape and rolling resistance. Railway Engineering Science, 2020, 28: 382-407.
[50] Li L, Liu W, Ma M, et al. Research on the dynamic behaviour of the railway ballast assembly subject

to the low loading condition based on a tridimensional DEM-FDM coupled approach. Construction and Building Materials, 2019, 218: 135-149.

[51] Indraratna B, Thakur PK, Vinod JS. Experimental and numerical study of railway ballast behavior under cyclic loading. International Journal of Geomechanics, 2010, 10(4): 136-144.

[52] Lobo-Guerrero S, Vallejo LE, Vesga LF. Visualization of crushing evolution in granular materials under compression using DEM. International Journal of Geomechanics, 2006, 6(3): 195-200.

[53] Johnson KL. Contact mechanics. Cambridge University Press, Cambridge, 1985.

[54] Hertz H. Ueber die Berührung fester elastischer Körper. Journal für die reine und angewandte Mathematik, 1882, 92: 156-171.

[55] Mortensen J, Faurholt JF, Hovad E, et al. Discrete element modelling of track ballast capturing the true shape of ballast stones. Powder Technology, 2021, 386: 144-153.

[56] Guo Y, Zhao C, Markine V, et al. Calibration for discrete element modelling of railway ballast: A review. Transportation Geotechnics, 2020, 23: 100341.

[57] Zhang X, Thompson D, Jeong H, et al. Measurements of the high frequency dynamic stiffness of railway ballast and subgrade. Journal of Sound and Vibration, 2020, 468: 115081.

[58] Liu G, Cong J, Wang P, et al. Study on vertical vibration and transmission characteristics of railway ballast using impact hammer test. Construction and Building Materials, 2022, 316: 125898.

[59] Jing G, Wang J, Wang H, et al. Numerical investigation of the behavior of stone ballast mixed by steel slag in ballasted railway track. Construction and Building Materials, 2020, 262: 120015.

[60] Esmaeili M, Askari A. Laboratory investigation of the cyclic behavior of rock ballast mixed with slag ballast for use in railway tracks. Construction and Building Materials, 2023, 365: 130136.

[61] Zhang X, Zhao C, Zhai W. Dynamic behavior analysis of high-speed railway ballast under moving vehicle loads using discrete element method. International Journal of Geomechanics, 2017, 17(7): 04016157.

[62] Bian X, Li W, Qian Y, et al. Micromechanical particle interactions in railway ballast through DEM simulations of direct shear tests. International Journal of Geomechanics, 2019, 19(5): 04019031.

[63] Coetzee CJ. Calibration of the discrete element method and the effect of particle shape. Powder Technology, 2016, 297: 50-70.

[64] Wong CP, Coop MR. The contact mechanics of a UK railway ballast. Géotechnique. 2024. 74(13): 1700-1712.

[65] Altuhafi FN, Coop MR. The small-strain stiffness of a railway ballast. Géotechnique, 2024, 74(12): 1475-1486.
[66] Altuhafi FN, Baudet BA, Coop MR. Plastic deformation effect on contact behaviour in granular materials. Granular Matter, 2024, 26(2): 34.
[67] Watson G, Piazza J, Madhusudhan BN, et al. Measuring the contact stiffness at the grain scale of fresh and used granite ballast. Advances in Transportation Geotechnics IV: Proceedings of the 4th International Conference on Transportation Geotechnics Volume 2. Springer International Publishing, 2022: 483-495.
[68] Gupta A, Madhusudhan BN, Zervos A, et al. Grain characterisation of fresh and used railway ballast, Granular Matter, 2022, 24(4): 96.
[69] Tutumluer E, Wang H, Husain SF, et al. A comparative study of new ballast and recycled ballast generated from various maintenance activities, Transportation Engineering, 2025, 20: 100321.
[70] Wang H, Husain SF, et al. A comparative study of new ballast and recycled ballast generated from various maintenance activities, Transportation Engineering, 2025, 20: 100321.
[71] Cole DM, Peters JF. A physically based approach to granular media mechanics: grain-scale experiments, initial results and implications to numerical modeling. Granular Matter, 2007, 9(5): 309-321.
[72] Cole DM, Peters JF. Grain-scale mechanics of geologic materials and lunar simulants under normal loading. Granular Matter, 2008, 10(3): 171-185.
[73] Milne D, Masoudi A, Ferro E, et al. An analysis of railway track behaviour based on distributed optical fibre acoustic sensing. Mechanical Systems and Signal Processing, 2020, 142: 106769.
[74] Watson G, Ferro E, Le Pen L, et al. Field scale trial of fibre-reinforced ballast. Advances in Transportation Geotechnics IV: Proceedings of the 4th International Conference on Transportation Geotechnics Volume 1. Cham: Springer International Publishing, 2021: 503-513.
[75] Christaras B, Auger F, Mosse E. Determination of the moduli of elasticity of rocks. Comparison of the ultrasonic velocity and mechanical resonance frequency methods with direct static methods. Materials and Structures, 1994, 27: 222-228.
[76] Yang B, He M, Zhang Z, et al. Experimental investigation and empirical model on damping properties of rock under multistage cyclic loading. Soil Dynamics and Earthquake Engineering, 2022,163: 107557.
[77] He M, Zhang Z, Li N. Experimental investigation and empirical model to determine the damping and shear stiffness properties of soft rock under multistage cyclic loading. Soil Dynamics and Earthquake

Engineering, 2021, 147: 106818.

[78] Qin Y, Xu X, Yan C, et al. Dynamic damping ratio of mudded intercalations with small and medium strain during cyclic dynamic loading. Engineering Geology, 2021, 280: 105952.

[79] Hashiguchi K. Constitutive equations of elastoplastic materials with elastic-plastic transition. ASEM Journal of applied mechanics, 1980, 47(2): 266-272.